New Printed-Circuit-Board Resonators with High Quality Factor and Transmission Efficiency for Mega-Hertz Wireless Power Transfer Applications

Kerui Li, *Member IEEE*, Jiayang Wu, *Member, IEEE*, Abdulkadir C. Yucel, *Senior Member*, and Shu-Yuen Ron Hui, *Fellow IEEE*

***Abstract*— This paper presents a new printed-circuit-board (PCB) resonator structure suitable for mega-Hertz wireless power transfer (WPT) applications. Unlike previous PCB resonators that can form only parallel resonant structures, the new designs can easily be configurated as either parallel or series resonators. The novelty of the resonator structure involves the replacement of the PCB material with an airgap in the main magnetic flux path of the resonator structure and adoption of air-trenches between adjacent turns, therefore greatly reducing the inter- and intra-capacitance of the two printed windings and its associated PCB dielectric power loss. The natural resonant frequency can easily be tuned for mega-Hertz operation. A comparative study is conducted between conventional and new designs. The quality factor, resonant frequency, transmission efficiency and ac resistance of the new designs are significantly improved by over 435%, 236%, 137% and 41%, respectively over those of the conventional designs. An accurate distributed-circuit model of the new PCB resonator structures is also included and used in domino WPT system simulation. PCB resonators of the conventional and new designs are constructed to form domino WPT systems for practical evaluation. Both simulation and practical results are included to confirm the accuracy of the PCB resonator model and the advantages of the new resonator structure.**

***Index Terms*— wireless power transfer, printed-circuit-board resonators, planar magnetics.**

I. INTRODUCTION

WITH the improvement of power electronics such as power MOSFETs in the 1980s, the switching frequency of switched mode power supplies could be increased from tens to hundreds of kilohertz to reduce the size of magnetics (such as isolation transformers) and increase power density [1]. In 1998, it was demonstrated that the magnetic cores in isolation transformers can be eliminated with the use of coreless PCB transformers for both power and signal transfer when the operating frequency exceeds a few hundred kilohertz [2]. Removal of magnetic cores has the advantages of not only eliminating the cost and size of magnetic cores but also the frequency limitations and power losses of the magnetic cores [3][4]. For these reasons, coreless PCB transformers could be operated beyond the Mega-Hertz frequency range [5][6] over 20 years ago. With such advantages, coreless PCB transformers are attractive to power integrated circuit companies and have been adopted in a family of industrial gate drive circuits for both individual power switches and inverter bridges since early 2000s [7]-[9]. The invention of operating method of coreless PCB transformer in [2] has led to a series of related patents with industrial applications [10]-[12]. Besides using PCB technology, the coreless planar transformer can in principle be manufactured in semiconductor technology [13] if the resistance of the coils can be kept to an acceptable level.

In recent years, research works on coreless PCB winding structures appear in medium-voltage and high-voltage gate drives [14], isolation transformers for multi-Mega-Hertz power supplies [15] and domino resonators for WPT applications [16]-[19]. The PCB winding structures are particularly important for domino WPT systems in the high-voltage (HV) insulation rod applications in HV transmission towers [19]. Power companies have confirmed that manual windings and discrete capacitors are not suitable for such HV applications because of the HV discharge between metallic terminals in discrete capacitors [20]. PCB resonator structures have distributed inductance and capacitance and can therefore avoid internal HV discharge [19]. For domino WPT applications, reference [19] reports a PCB resonator winding design optimized by the partial-element equivalent-circuit (PEEC) method. However, the PCB resonator structures in [19] and [20], when manufactured to the size for embedment inside standard insulation discs of commercial insulation rods, have limitations on operating frequency range and relatively low quality (Q) factor and energy efficiency due to the dimensions of the PCB. In addition, these structures are restricted to parallel resonant

Manuscript received Month xx, 2xxx; revised Month xx, xxxx; accepted Month x, xxxx. This work was supported by the A*Star MTC Individual Research Grant M21K2c0108. (Corresponding author: Shu Yuen Ron Hui).

Kerui Li is with the Department of Electrical and Electronic Engineering, The Hong Kong Polytechnic University, Hong Kong SAR (e-mail: kerui.li@polyu.edu.hk).

Jiayang Wu is with the School of Electrical and Electronic Engineering, Nanyang Technological University, Singapore 639798 (e-mail: jiayang.wu@ntu.edu.sg).

Abdulkadir C. Yucel is with the School of Electrical and Electronic Engineering, Nanyang Technological University, Singapore 639798 (e-mail: acyucel@ntu.edu.sg).

Shu Yuen Ron Hui is with the School of Electrical and Electronic Engineering, Nanyang Technological University, Singapore 639798, and also with Department of Electrical and Electronic Engineering, Imperial College London, London SW7 2BX, U.K. (e-mail: ron.hui@ntu.edu.sg).

Color versions of one or more of the figures in this article are available online at http://ieeexplore.ieee.org

configurations. Traditional PCB resonators have two planar windings printed on the two sides of a PCB board and the PCB material in between is used for dielectric. At mega-Hertz operation, the dielectric power loss of the PCB material becomes significant [21]-[23].

In this paper, new PCB resonator designs are proposed [24] for significant advancement over existing designs. This paper is an extended version of a conference paper [25]. Taking advantages of the low dielectric constant of air, the new resonator structure uses the airgap to separate the two printed planar windings of the resonator. Compared with conventional designs [19],[20], the new PCB resonator design has the following advantages:

1) replacing the PCB material (with a typical dielectric constant of 4.2 and loss tangent of 0.03) with an airgap (with a dielectric constant of 1.0 and virtually zero loss tangent), therefore greatly reducing the inter-capacitance and its associated dielectric power loss of the resonator,
2) the flexibility of being configurated as either series or parallel resonators,
3) have much high resonant frequency due to the reduction of inter-capacitance in 1),
4) have much higher Q factor due to the reduction of ac winding resistance,
5) have significant improvement in transmission efficiency.

Section II describes the structural differences among the conventional PCB resonator design and two proposed PCB resonator designs. In the three cases, the winding patterns are printed on the PCBs of the same dimensions. Accurate models of the proposed PCB resonator designs are included and explained in Section III. Section IV presents the theoretical and practical characteristics of the three designs. Based on the same test platform of a domino WPT system, the three PCB resonator designs are tested for their transmission efficiency. A comparison of the Q factor, bandwidth, ac winding resistance and transmission efficiency is included to confirm the advantages of the proposed PCB resonator structures.

II. Conventional And Novel PCB Resonator Structures

References [19] and [20] use PCB windings printed on the two sides of circular PCB discs as the relay resonators in domino WPT systems. It is demonstrated in [19], [26], [27] that printed spiral winding with variable width has low resistance. To provide a common platform for comparison, the spiral and planar PCB windings with variable widths are printed as resonators in this study. Each PCB has a dimeter of 21cm and the outermost circular winding a dimeter of 20cm. The printed windings for the conventional design and the two new designs are first optimized using the COMSOL electromagnetic design software to maximize the Q factor:

$$Q = \frac{f_o}{\Delta f} \tag{1}$$

where f_o is the resonant frequency and Δf is the 3dB bandwidth.

In this comparative study, the three PCB resonator structures are summarized as follows:

1) The conventional PCB resonator design is adopted from optimized design in [19], with the two PCB windings printed on the two sides of the same PCB board. The dielectric material between the two planar PCB windings is the standard FR-4 PCB material. The dielectric constant of the FR-4 PCB is typically 4.2.
2) New Design-1 is based on the same conventional PCB windings in [19] except that the two planar PCB windings are printed on two different PCB boards arranged in a co-axial manner and separated with a new and uniform airgap to reduce the inter-winding capacitance. The dielectric constant of air is 1.0.
3) New design-2 retains the two-layer structure of Design-1, but the two PCB windings are optimized specifically for the two-layer structure with an airgap between the two planar PCB windings and with air-trenches between adjacent turns to further reduce the intra-winding capacitance.

The sandwiched structure utilized in the new design has extremely low dielectric loss. In addition, the copper loss is also minimized through the careful selection of trace width such that the current can be evenly distributed along the PCB traces. According to the finite element simulation results, the current near the connectors (or via in the conventional design) is relatively high and the current decreases along the copper trace. As a result, a wider trace width is used for the outer turns near the connectors to reduce the copper loss. The specific values for the trace width are optimized by using finite element simulation.

In reference [28], a Bayesian optimization framework has been proposed for parallel resonators. To fit the framework, the PCB resonator is reconfigured as parallel compensation. Fig. 1(a) shows the design variables of the n-turn PCB coil, in which the radius of the outermost trace r_{out}, the radius of the innermost copper trace r_{in}, the distance between two adjacent trace d, and the trace width of each turns w_1, w_2, …, w_n are used. It is worth noting that proportional trace width is adopted, i.e., $w_2/w_1=w_3/w_2\ldots=w_n/w_{n-1}=k$. With the ratio k, trace width of the first trace w_1, and the number of turns n, the trace width of the n-turn PCB coil can be automatically generated. The use of proportional trace width can effectively reduce the number of unknown variables and expedite the optimization process. The flowchart of the optimization process is shown in Fig. 1 (b). In this optimization process, r_{out} is set at 100 mm, and the constraints of the other optimization variables are set as $r_{in} \in$ [26 mm, 70 mm], $w_1 \in$ [0.5 mm, 15 mm], $k \in$ [0.8, 1.2], $d \in$ [0.5 mm, 4 mm], $n \in$ [1 turn, 100 turns].

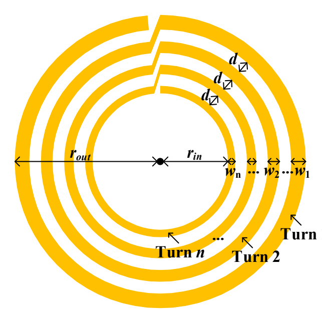

(a) Design variables for copper traces

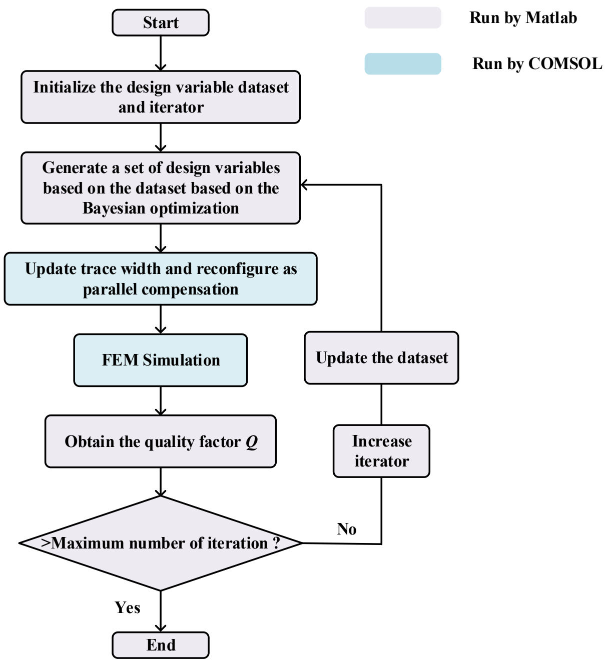

(b) Flowchart of the optimization process

Fig. 1. Flowchart of the optimization process.

After starting the optimization process, the design variables dataset and iterator are initialized. A set of feasible design variables are then generated based on the dataset. Then the design variables are then converted into specific trace width of the PCB resonator. The trace width is sent to COMSOL simulation software to update the 3D structure. In addition, the PCB resonator is reconfigured as parallel compensation by short-circuiting the input-output terminals. The quality factor of the PCB resonator can be directly obtained by running the eigenfrequency study. Finally, the resulting quality factor and trace width are used to update the dataset. The optimization process ends if the iterator exceeds the maximum number of iterations. Another factor affecting the Q factor is the loss tangent of the PCB materials. Table I compares the relative permittivity, loss tangent and costs of a common PCB, high-frequency PCB, and air. Note that the relative permittivity of PCB materials is typically over three times that of air. As the price of the high-frequency PCB materials is much higher than the ordinary type, this study will use the FR-4 PCB material as the comparison platform.

TABLE I
COMPARISON OF COMMON PCB, HIGH-FREQUENCY PCB AND AIR

Material	FR-4 (Common PCB)	Rogers RO4350B (High-frequency PCB)	Air
Relative permittivity ε_r	3.3-4.8	3.48 ± 0.05	1
Loss tangent	0.02 – 0.03	0.0037	0
Unit cost for 100 pieces 1oz PCB with dimension of 210mm×210mm*	4.79 USD/piece	72.22 USD/piece	N/A

A. Conventional PCB Resonators

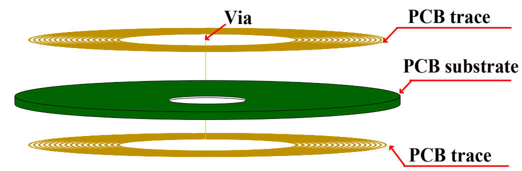

Fig.2. Structure of a conventional PCB resonator with two spiral windings printed on two sides of the PCB and connected through a via.

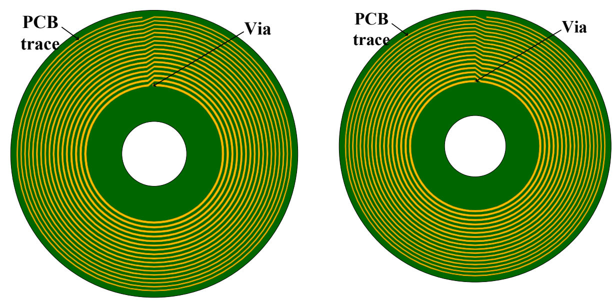

(a) Front view (b) Back view

Fig. 3. Winding patterns of the conventional PCB resonator.

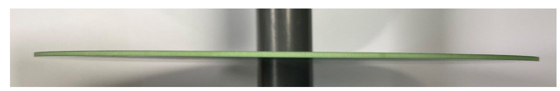

Fig. 4. Side view of the conventional resonator.

Fig. 2 shows the structure of the conventional PCB resonator. It consists of two printed spiral windings on the two sides of the same PCB. The two spiral windings are connected through a via. Based on the optimization procedure described in Fig. 1, the winding patterns on the two sides of the PCB are shown in Fig. 3. The two spiral windings form the distributed inductor, which accounts for the magnetic field created in the winding structure whenever there is a current in the winding. The main distributed capacitance is provided by the electric field between the copper tracks between the two sides of the PCB. The electric field appears across the PCB material with a relative permittivity of typically 3.3 to 4.8 (Table I). There is also (stray) intra-capacitance between adjacent copper tracks on the same side of the PCB. The side view of the conventional PCB resonator is shown in Fig. 4. Note that the conventional PCB resonator in Fig. 2 is inherently a parallel resonant tank. It can only be re-configurated into a series resonant tank when the via connection between the two spiral coils printed on both sides of the PCB is removed.

B. New PCB Resonator (Design-1)

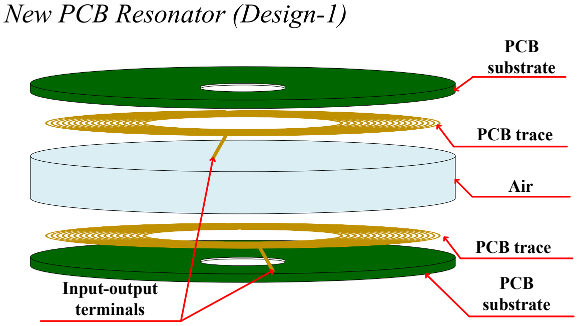

Fig. 5. Structure of a new design of PCB resonator based on two separate PCBs with an airgap (Design-1).

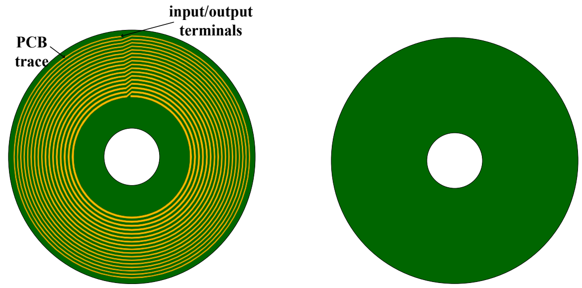

(a) Front view (b) Back view

Fig. 6. Winding patterns of the one of the two PCBs for a new PCB resonator.

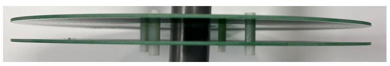

Fig. 7. Side view of a new PCB resonator design (Design-1) formed by two PCBs with an airgap, with the printed coils facing each other.

The capacitance between the printed spiral coils on the two sides of the PCB is affected by the permittivity of the PCB materials in the conventional PCB resonator structure in Fig. 2. Table I indicates that the permittivity of the PCB materials is higher than that of air. Therefore, the inter-capacitance between the two printed spiral coils can be reduced if the two printed coils are printed on two separate PCBs and are separated by an airgap as shown in the new design (labeled as Design-1) in Fig. 5. For Design-1, the two PCBs originally optimized for the conventional design are used to form the new resonator with one spiral coil printed on each PCB as shown in Fig. 6. The corresponding side view is shown in Fig. 7. With the material between the two printed coils changed from PCB materials to air, the inter-capacitance of the resonator can be reduced, therefore increasing the resonant frequency of the resonator. Since the energy efficiency of the resonator increases with the Q factor and operating frequency, Design-1 is expected to offer a higher energy efficiency as would be seen in the next section.

C. New PCB Resonator (Design-2)

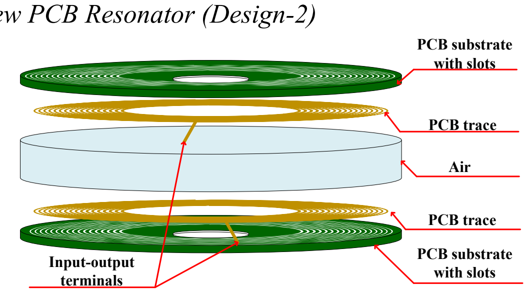

Fig. 8. Structure of a new design of PCB resonator based on two PCBs separated with an airgap, and with air trenches between adjacent turns on each PCB (Design-2).

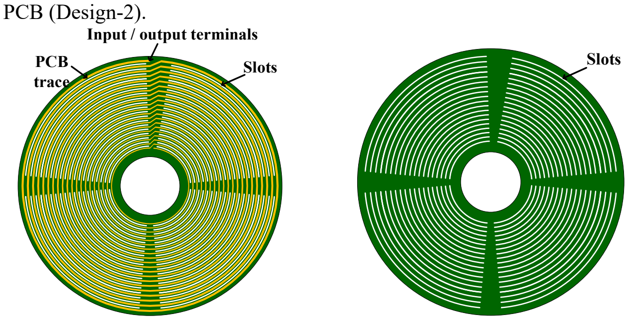

(a) Front view (b) Back view

Fig. 9. Winding patterns of one of the two PCBs for a new PCB resonator (Front view showing spiral coil with trenches or air slots) between adjacent turns; back view has no printed coil)

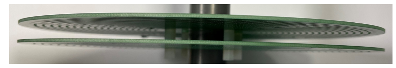

Fig. 10. Side view of a new PCB resonator design (Design-2) formed by two PCBs with an airgap.

Unlike Design-1 which uses the winding designs optimized for the conventional design, Design-2 is optimized for its two-layer structure with the COMSOL software for maximum Q factor. Therefore, it has different number of turns (Table II). The structure of Design-2 is further improved by reducing the intra-capacitance between adjacent turns of the printed spiral coil by removing some part of PCB material between the adjacent turns to form air trenches. Fig. 8 shows the structure of this improved design (Design-2). Similar to that of Design-1, the resonator structure is formed by two PCBs, with one printed spiral coil on each PCB. The two PCBs are separated by an airgap to reduce the inter-capacitance. Design-2 has less intra-capacitance because of the formation of trenches (with the PCB materials removed) as shown in Fig. 9. Note that not all PCB material between adjacent turns is removed, because it is necessary to use some PCB material to keep the printed coil in the spiral structure. The side view of Design-2 is included in Fig. 10. The extra advantages of Design-2 over Design-1 and the conventional PCB resonator will be illustrated in the next sections.

III. Accurate Modeling and Practical Verification of the Three PCB Resonator Structures

Table II summarizes the parameters of three PCB resonators structures.

TABLE II
PARAMETERS OF PCB RESONATORS STRUCTURES

		Conventional design	Design 1	Design 2
Copper trace parameters	First turn trace width w_1	0.701 mm	0.701 mm	1.626 mm
	Radius of the outermost trace r_{out}	99 mm	99 mm	100 mm
	Radius of the innermost trace r_{in}	46.211 mm	46.211 mm	26.971 mm
	Trace width ratio between two adjacent turns k	1.044	1.044	0.963
	Number of turns n	17	17	20
	Distance between trace	2.059 mm	2.059 mm	2.482 mm
	Slots width	N/A	N/A	1 mm
PCB thickness		1.6 mm	1.6 mm	1.6 mm
Copper thickness		1 oz	1 oz	1 oz
Distance between two PCBs		N/A	5 mm	5 mm

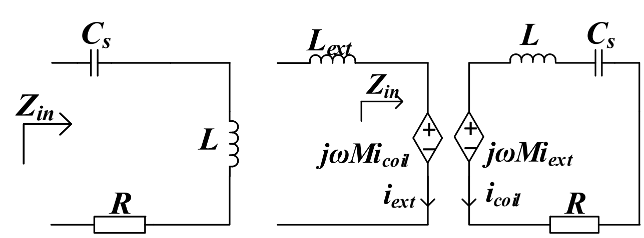

(a) (b)

Fig. 11. (a) Second-order circuit and (b) equivalent circuit for a WPT system with secondary parallel resonant circuit.

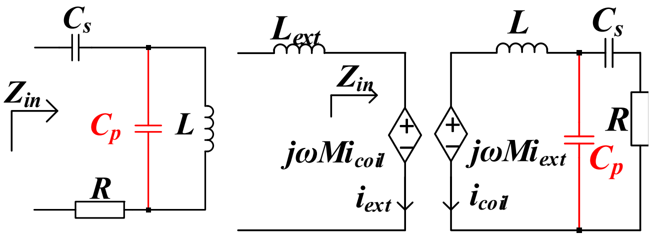

(a) (b)

Fig. 12. (a) Third-order circuit and (b) equivalent circuit for a WPT system with secondary parallel resonant circuit.

The two new PCB resonator designs are tested and compared with the conventional structure in two ways. Firstly, their impedance-frequency characteristics, resonant frequencies and Q factors are modeled, measured and compared. Secondly, the three PCB resonator structures are used to form three domino WPT systems with the same transmission distance so that their transmission efficiencies can be measured and compared.

The traditional lumped-element equivalent circuit for inductive-capacitive (LC) resonators is to use a second-order circuit as shown in Fig. 11. But for printed resonators, both of the inductance and capacitance are distributed. More importantly, it is necessary to consider both the inter-capacitance (C_s) and the intra-capacitance (C_p) of the winding structures because the resonant frequency would be in the Mega-Hertz range. For this reason, an extra capacitor is added in a third-order resonant circuit to represent the intra-capacitance as shown in Fig. 12.

A. Characteristics of the three PCB Resonator Structures

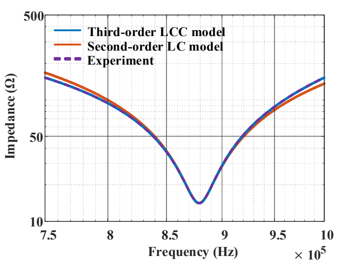

(a) Input impedance of the conventional PCB resonator structure when it is converted into "series" resonator

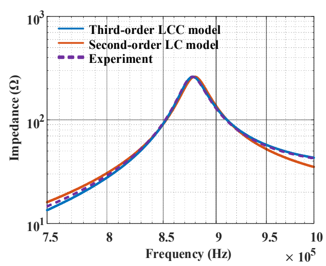

(b) Input impedance of the conventional PCB resonator structure as seen from a transmitter coil.

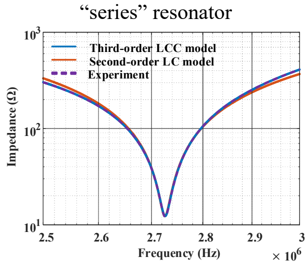

(c) Input impedance of the Design-1 structure.

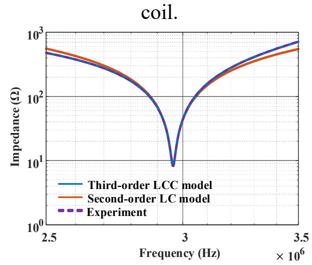

(d) Input impedance of the Design-2 structure.

Fig. 13. Measured and theoretical impedance plots of the three PCB resonator structures.

The impedance-frequency plots of the three different PCB resonator structures are practically measured and compared with the simulated results based on the second-order and third-order circuit models (Fig. 13).

The impedance of the conventional PCB resonator, being a closed-loop "parallel" resonator, cannot be measured directly. To measure such impedance, the resonator is first transformed into a "series" configuration by removing the via that connects the top and bottom copper layers and using the via's terminals as the input and output ports of the resonator. For the structures of Design-1 and Design-2, they can be configurated as "series" resonators for direct measurement. After configurating the resonators as "series" resonators, the impedance-frequency plots Z_{in_data} of these resonators can be measured with an impedance analyzer directly.

The quality factor Q and the resonant frequency f_0 can be directly obtained from the impedance data Z_{in_data}. The parameters of second-order model are derived based on the definition of Q

$$R = \left|Z_{in\_data}(2\pi f_0)\right| \tag{2}$$

$$L = \frac{QR}{2\pi f_0} \tag{3}$$

$$C = \frac{1}{(2\pi f_0)^2 L} \tag{4}$$

The parameters of third-order model are derived by solving the optimization problem as

$$\underset{L,R,C_s,C_p}{\operatorname{argmin}} \left\| \left| \frac{1}{sC_s} + \frac{1}{{}^{1}\!/_{sL} + sC_p} \right| - \left|Z_{in\_data}\right| \right\|_2 \tag{5}$$

The characteristics of the three resonator structures are tabulated in Table III.

The simulated and measured impedance-frequency plots are shown in Fig. 13. Fig. 13 (a) shows the results for the conventional PCB resonator when it is converted into a "series" resonator and Fig. 13 (b) shows the input impedance of the conventional design as seen from a transmitter coil. Fig. 13 (c) and Fig. 13 (d) show the input impedance for Design-1 and Design-2 as "series" resonators, respectively.

In all three cases, the simulated results of the third-order circuit models fit very well with the measured ones. The simulated results of the second-order model deviate increasingly from practical measurements as the frequency moves away on both sides from the respective resonant frequencies. Therefore, the third-order equivalent circuit should be used for analysis of PCB resonators.

B. Comparison of parameters of the three PCB Resonator Structures

TABLE III
COMPARISON OF MEASURED RESONATOR PARAMETERS

		Conventional design	Design 1	Design 2
Q and f_0		37.069 @ 879.107 kHz	156.055 @ 2.726 MHz	198.574 @ 2.961MHz
Number of turns		17	17	20
Second -order model	L (μH)	94.679	112.09	87.825
	C_s (pF)	346.180	30.412	32.883
	R (Ω)	14.108	12.302	8.230
Third-order model	L (μH)	50.528	46.191	35.521
	C_s (pF)	473.848	47.693	51.682
	C_p (pF)	174.705	26.083	29.642
	R (Ω)	14.108	12.302	8.230

From Table III, the Q factor of the conventional resonator is 37.1 at the resonant frequency of 879 kHz. The Q factors of the Design-1 and Design-2 are 156.1 at a resonant frequency of 2.73 MHz and 198.6 at 2.96 MHz, respectively. The improvements in the Q factor are therefore 4.21 times in Design-1 and 5.35 times in Design-2. The resonant frequencies change from 879 kHz in the conventional structure to 2.73 MHz in Design-1 and 2.96 MHz in Design-2. The increase in the resonant frequencies is due mainly to the reduction in the self-inductance and the inter-capacitance. The equivalent winding resistances of Design-1 and Design-2 are smaller than that of the conventional design. The comparative results in Table III confirm that the two new PCB resonator structures, namely Design-1 and Design-2, have superior characteristics than the conventional one.

C. Loss mechanism and comparison

The dielectric loss of the PCB capacitor is associated with the dissipation factor of the dielectric material. In conventional PCB resonator designs, the displacement current flows through the high-loss FR-4 substrate, leading to high dielectric losses, as shown in Fig. 14(a). In contrast, Design-1 and Design-2 redirect the displacement current to flow through the air, as demonstrated in Fig. 14(b) and (c), respectively. This design modification results in lower dielectric losses for Design-1 and Design-2 compared to the conventional design.

The ohmic loss of the resonator is affected by the skin effect and proximity effect of the PCB traces. In conventional design, the surface current density of inner turns is higher (Fig. 15(a)). In contrast, in Design-1 and Design-2, the outer turns display higher surface current density (Fig. 15(b) and (c)). To reduce the ohmic loss, wider trace widths are utilized for the outer turns in Design-2, resulting in a lower ohmic loss. In summary, given the reduced dielectric loss and ohmic loss, Design-2 achieves the highest quality factor among these three designs.

Finite element simulations with COMSOL software are performed to quantitatively assess the loss of the resonators. Two sets of simulations are performed. A practical resonator based on a PCB substrate FR-4 (with a loss tangent of 0.017) is used in the first simulation. In the second simulation, the loss tangent of the same PCB substrate is artificially set to zero. By performing adaptive frequency sweeping, the impedance curves of the resonators are obtained, and the parameters of the third-order model are obtained based on (5). By comparing the parameters in two sets of simulations, we were able to separate the load resistance contributed by the PCB substrate (R_{PCB}) and copper trace (R_{copper}), as shown in Fig. 16. The corresponding results are summarized in Table IV.

When comparing the R_{PCB} among these designs, it becomes evident that the reduction in dielectric loss is the primary reason for the superior performance of Design-1 and Design-2 over the conventional design. Additionally, by removing the PCB substrates between adjacent turns and optimizing the trace widths, Design-2 achieves a significant reduction in both dielectric loss and ohmic loss, resulting in a lower R_{PCB} and R_{copper}, and eventually leading to the highest quality factor among the three designs.

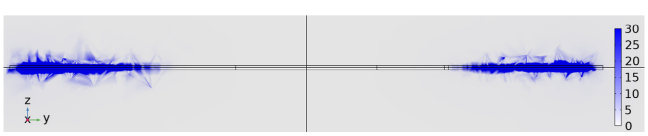

(a) Conventional design

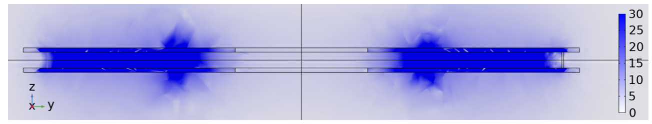

(b) Design-1

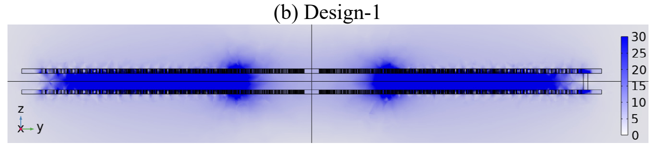

(c) Design-2

Fig. 14. Displacement current density (unit: A/m^2) of the resonators operating at f_0.

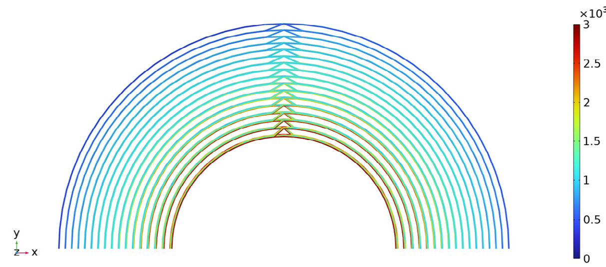

(a) Conventional design

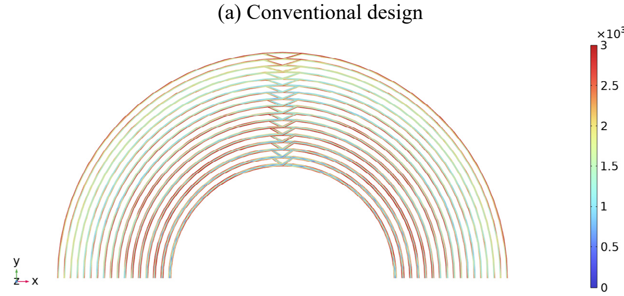

(b) Design-1

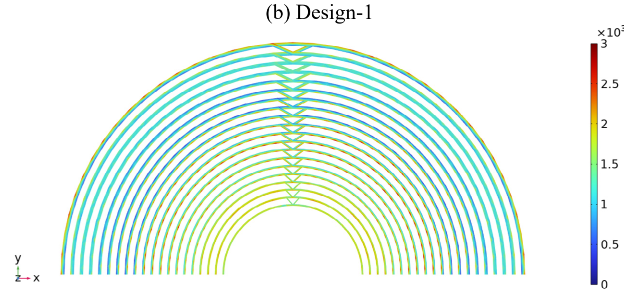

(c) Design-2

Fig. 15. Surface current density (unit: A/m) of the resonators operating at f_0.

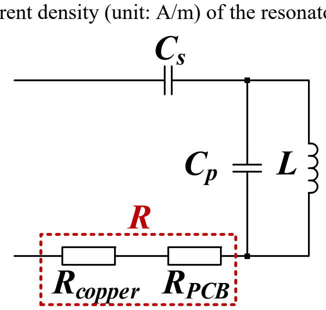

Fig. 16. Equivalent circuit model of the resonator with separated load resistance.

TABLE IV
COMPARISON OF RESONATOR PARAMETERS BASED ON FINITE ELEMENT SIMULATIONS

		Conventional design	Design 1	Design 2
	L (μH)	53.1	49.4	38.5

Loss tangent=0.017	C_s (pF)	465	44.7	49.1
	C_p (pF)	169	22.8	24.5
	$R_{copper}+R_{PCB}$ (Ω)	14.7	13.6	8.53
Loss tangent=0	L (μH)	53.1	49.4	38.5
	C_s (pF)	465	44.7	49.1
	C_p (pF)	169	22.8	24.5
	R_{copper} (Ω)	6.30	11.1	7.87
Summary	R_{PCB} (Ω)	8.43	2.5	0.66
	R_{copper} (Ω)	6.30	11.1	7.87

IV. Comparison of Transmission Efficiency in Domino WPT Systems

The three different PCB resonator structures are configurated to form 4-coil domino WPT systems as shown in Fig. 17. The first and the fourth PCB resonators are configurated into series-resonator. The second and the third resonators are parallel-resonators, and are used as relay resonators. The distance between adjacent PCB resonators is kept the same in these domino WPT systems. The matrix system equations for the 4-coil domino WPT system are shown in (6) and (7).

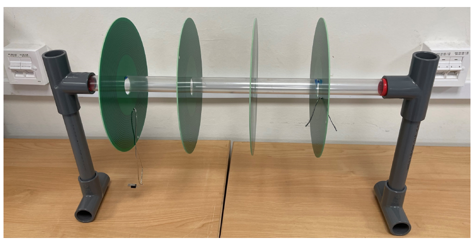

(a) Conventional design

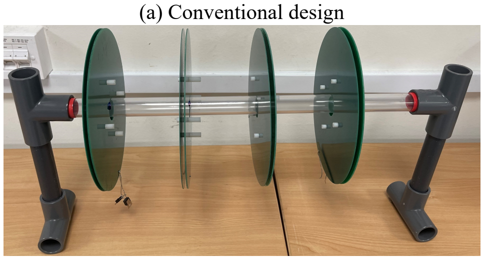

(b) Design 1

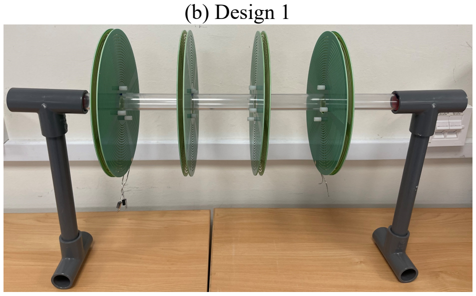

(c) Design 2

Fig.17. The 4-coil domino WPT systems.

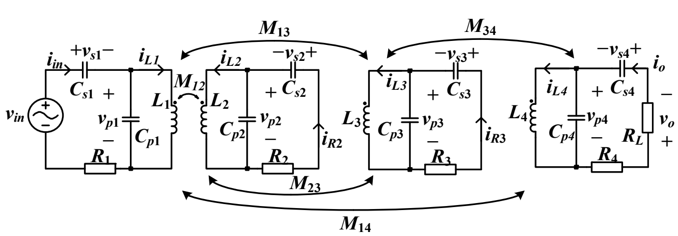

Fig.18. Equivalent circuit model of the 4-coil domino WPT system.

The state-space matrix equations for the 4-coil domino WPT system are derived as

$$\begin{bmatrix}\frac{di_{L\_matrix}}{dt}\\ \frac{dv_{p\_matrix}}{dt}\\ \frac{dv_{s\_matrix}}{dt}\end{bmatrix} = \begin{bmatrix} \mathbf{0} & \mathbf{L}_{matrix}^{-1} & \mathbf{0} \\ -\mathbf{C}_{p\_matrix}^{-1} & -\mathbf{C}_{p\_matrix}^{-1}\mathbf{R}_{matrix}^{-1} & -\mathbf{C}_{p\_matrix}^{-1}\mathbf{R}_{matrix}^{-1}\\ \mathbf{0} & -\mathbf{C}_{s\_matrix}^{-1}\mathbf{R}_{matrix}^{-1} & -\mathbf{C}_{s\_matrix}^{-1}\mathbf{R}_{matrix}^{-1}\end{bmatrix}\begin{bmatrix}\mathbf{i}_{L\_matrix}\\ \mathbf{v}_{p\_matrix}\\ \mathbf{v}_{s\_matrix}\end{bmatrix} + \begin{bmatrix}\mathbf{0}\\ \mathbf{C}_{p\_matrix}^{-1}\mathbf{v}_{in\_matrix}\\ \mathbf{C}_{s\_matrix}^{-1}\mathbf{v}_{in\_matrix}\end{bmatrix} v_{in} \quad (6)$$

$$\begin{bmatrix} i_{in}\\ i_{R2}\\ i_{R3}\\ i_{R4}\end{bmatrix} = \begin{bmatrix}\mathbf{0} & -\mathbf{R}_{matrix}^{-1} & -\mathbf{R}_{matrix}^{-1}\end{bmatrix}\begin{bmatrix}\mathbf{i}_{L\_matrix}\\ \mathbf{v}_{p\_matrix}\\ \mathbf{v}_{s\_matrix}\end{bmatrix} + [\mathbf{v}_{in\_matrix}]v_{in} \quad (7)$$

where $\mathbf{L}_{matrix} = \begin{bmatrix} L_1 & M_{12} & M_{13} & M_{14}\\ M_{21} & L_2 & M_{23} & M_{24}\\ M_{31} & M_{32} & L_3 & M_{34}\\ M_{41} & M_{42} & M_{43} & L_4\end{bmatrix}$,

$\mathbf{C}_{s\_matrix} = \begin{bmatrix} C_{s1} & 0 & 0 & 0\\ 0 & C_{s2} & 0 & 0\\ 0 & 0 & C_{s3} & 0\\ 0 & 0 & 0 & C_{s4}\end{bmatrix}$,

$\mathbf{C}_{p\_matrix} = \begin{bmatrix} C_{p1} & 0 & 0 & 0\\ 0 & C_{p2} & 0 & 0\\ 0 & 0 & C_{p3} & 0\\ 0 & 0 & 0 & C_{p4}\end{bmatrix}$,

$\mathbf{R}_{matrix} = \begin{bmatrix} R_1 & 0 & 0 & 0\\ 0 & R_2 & 0 & 0\\ 0 & 0 & R_3 & 0\\ 0 & 0 & 0 & R_4+R_L\end{bmatrix}$,

$\mathbf{i}_{L\_martrix}=[i_{L1}(t), i_{L2}(t), i_{L3}(t), i_{L4}(t)]^T$, $\mathbf{v}_{s\_martrix}=[v_{s1}(t), v_{s2}(t), v_{s3}(t), v_{s4}(t)]^T$, $\mathbf{v}_{p\_martrix}=[v_{p1}(t), v_{p2}(t), v_{p3}(t), v_{p4}(t)]^T$, $\mathbf{v}_{in\_martrix}=[R_1^{-1}, 0, 0, 0]^T$, $\mathbf{0}$ is the 4×4 zero matrix, and v_{in} is a purely sinusoidal voltage source $v_{in}=V_{in}\sin(2\pi ft)$.

The efficiency of the domino system is written as

$$\eta = \frac{\frac{1}{T}\int_{\tau}^{\tau+T} i_o^2 R_L dt}{\frac{1}{T}\int_{\tau}^{\tau+T}[i_o^2(R_L+R_4)+i_{R3}^2R_3+i_{R2}^2R_2+i_{in}^2R_1]dt} \quad (8)$$

where T (=1/f) is the period of v_{in}, and τ is the starting time for efficiency calculation. To increase the accuracy of efficiency calculation, a sufficiently large τ is used such that the WPT system is operating at steady-state.

In this test, the distance between adjacent PCB resonator is 10 cm and the load of 4-coil domino WPT system R_L = 25 Ω. To lower the complexity of the model, some parameters of the PCB resonators in the 4-coil domino WPT system can be assumed to be identical, e.g., $L_1=L_2=L_3=L_4$, $C_{s1}=C_{s2}=C_{s3}=C_{s4}$, $C_{p1}=C_{p2}=C_{p3}=C_{p4}$ $R_1=R_2=R_3=R_4$. In addition, the mutual inductance between two PCB resonators with the same distance can be assumed to be identical, i.e., $M_{12}=M_{23}=M_{34}$, and $M_{13}=M_{24}$.

By fitting the experimental input impedance data Z_{in_data} of the 4-coil domino WPT system with 2-norm, the mutual inductance of the equivalent circuit model (see Fig. 18) can be obtained as:

$$\underset{M_{12},M_{13},M_{14}}{\operatorname{argmin}} \left\| \left| \frac{v_{in}(s)}{i_{in}(s)} \right| - \left| Z_{in_{data}} \right| \right\|_2 \quad (9)$$

By using the corresponding parameters of the PCB resonators in Table III, the resulting mutual inductance of the 4-coil domino WPT system are shown in Table V.

TABLE V
PARAMETERS OF THE 4-COIL DOMINO WPT SYSTEMS

	Conventional design	Design 1	Design 2
M_{12}	5.2878 μH	5.4519μH	5.2467 μH
M_{13}	1.2799 μH	1.4051μH	1.3801 μH
M_{14}	0.1520 μH	0.1452μH	0.8962 μH
M_{23}	5.2878 μH	5.4519μH	5.2467 μH
M_{24}	1.2799 μH	1.4051μH	1.3801 μH
M_{34}	5.2878 μH	5.4519μH	5.2467 μH

Figs. 19-21 show the frequency spectra of the input impedance of the 4-coil domino WPT system conventional design, Design-1, and Design-2, respectively. The impedance curves from the model are close to the experimental results. The accuracy of the model in frequency domain is verified.

To further verify the accuracy of the model, time-domain tests are performed. The amplitude of the AC excitation is V_{in}=50 V. The operating frequencies of these domino systems are 879 kHz, 2.72 MHz, and 2.96 MHz, corresponding to the self-resonant frequencies of the PCB resonators (see Table III). Figs. 22-24 show the time-domain waveforms of the 4-coil domino WPT system with conventional design, design 1, and design 2. The time domain waveforms from the model are very close to the experimental ones. The accuracy of the model in time domain is verified.

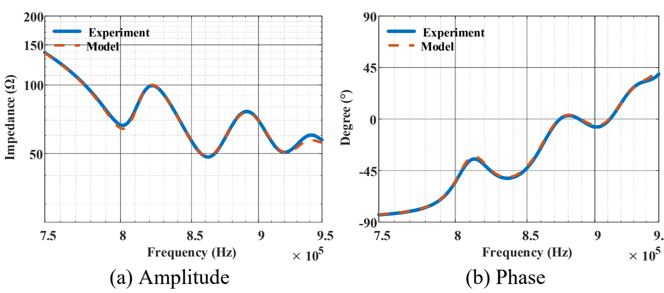

(a) Amplitude (b) Phase

Fig. 19. Input impedance of the 4-coil domino system with conventional design.

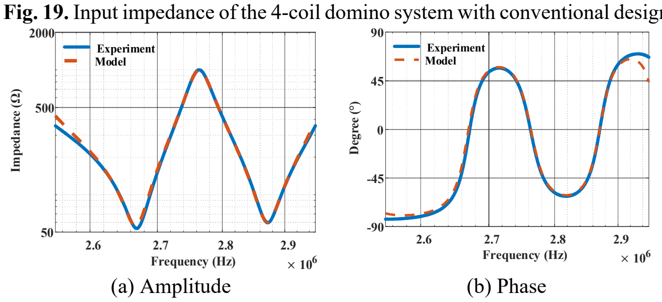

(a) Amplitude (b) Phase

Fig. 20. Input impedance of the 4-coil domino system with Design-1.

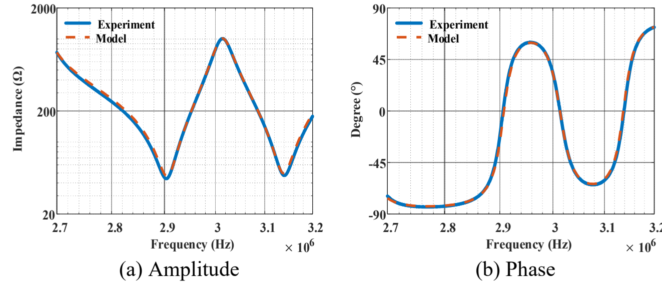

(a) Amplitude (b) Phase

Fig. 21. Input impedance of the 4-coil domino system with Design-2.

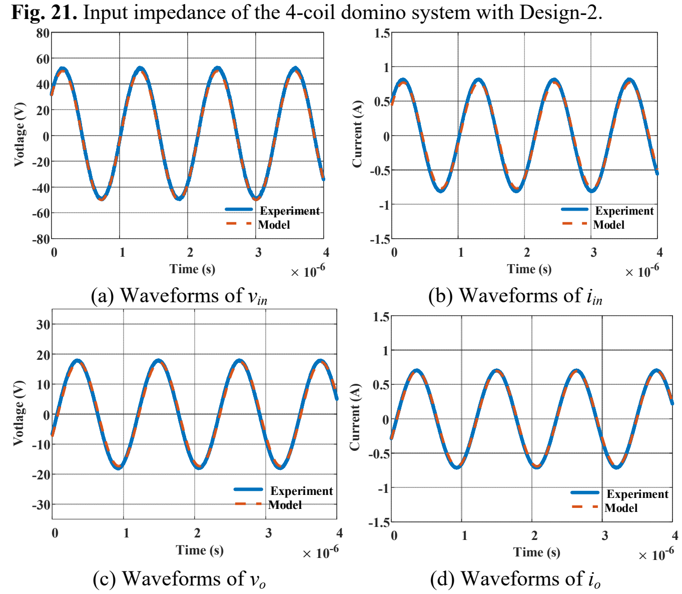

(a) Waveforms of v_{in} (b) Waveforms of i_{in}

(c) Waveforms of v_o (d) Waveforms of i_o

Fig. 22. Waveforms of the 4-coil domino system with conventional design.

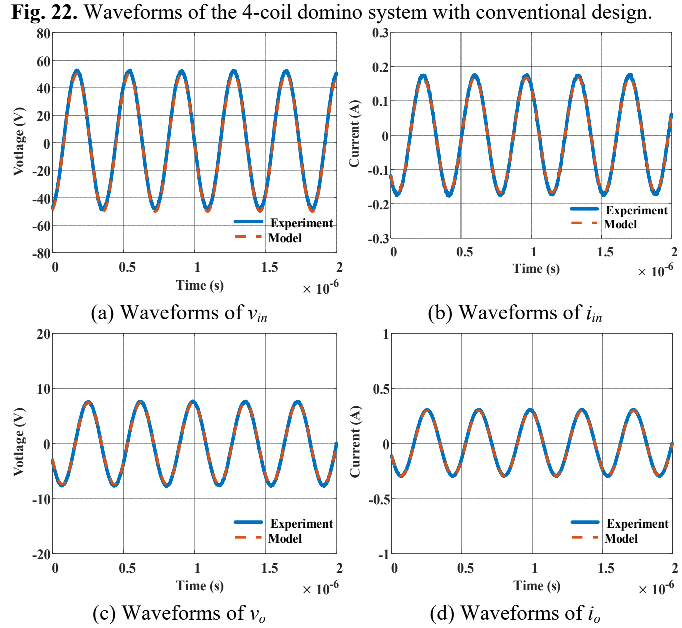

(a) Waveforms of v_{in} (b) Waveforms of i_{in}

(c) Waveforms of v_o (d) Waveforms of i_o

Fig. 23. Waveforms of the 4-coil domino system with Design-1.

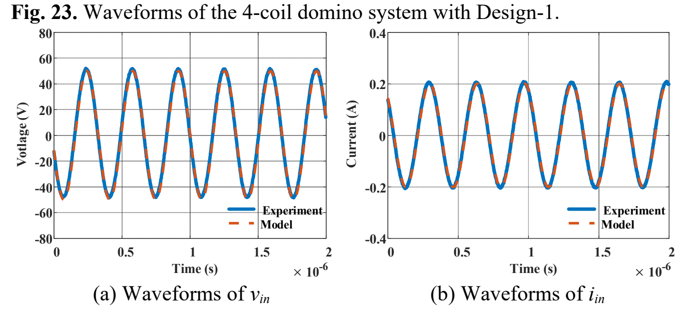

(a) Waveforms of v_{in} (b) Waveforms of i_{in}

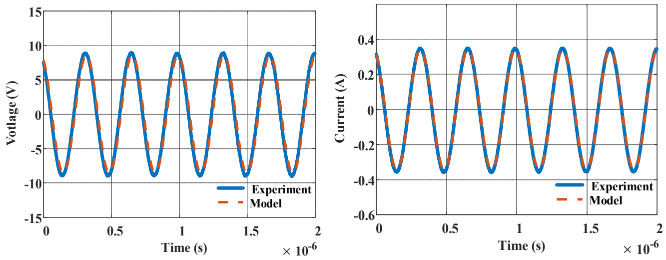

(c) Waveforms of v_o (d) Waveforms of i_o

Fig. 24. Waveforms of the 4-coil domino system with Design-2.

Based on the model, the optimal operating frequency and optimal load can be derived thorough solving the optimization problem as

$$
\begin{aligned}
&\underset{f,R_L}{\operatorname{argmin}} -\eta \\
&= \underset{f,R_L}{\operatorname{argmin}} \frac{-\int_{\tau}^{\tau+\frac{1}{f}} i_o{}^2 R_L \, dt}{\int_{\tau}^{\tau+\frac{1}{f}} [i_o{}^2(R_L + R_4) + i_{R3}{}^2 R_3 + i_{R2}{}^2 R_2 + i_{in}{}^2 R_1] dt} \\
&\qquad s.t. \begin{cases} f_{min} \le f \le f_{max} \\ R_{L\_min} \le R_L \le R_{L\_max} \end{cases}
\end{aligned} \tag{10}
$$

The maximum (f_{max}) and minimum frequencies (f_{min}) for the optimization are set as $1.05f_0$ and $0.95f_0$, while the maximum (R_{L_max}) and minimum load resistances (R_{L_min}) are set as 1000 Ω and 1 Ω. The MATLAB surrogate optimization solver is used to solve the optimization problem. The resulting optimal frequency and load for the conventional design are 851.715 kHz and 76.36 Ω, those for Design-1 are 2.744 MHz and 218.77 Ω, and those for Design-2 are 3.003 MHz and 201.77 Ω.

Fig. 25 (a)-(c) show the time-domain waveforms of the domino systems operating at the optimal frequency and load. In Fig. 25 (a), the waveform corresponds to the conventional design, where the peak-to-peak voltage of the AC input is 98.44 V. The input power, output power, and transmission efficiency of this system are 12.11 W, 4.395 W, and 36.29%, respectively. In Fig. 25 (b), the waveform corresponds to Design-1, where the peak-to-peak voltage of the AC input is 101 V. The input power, output power, and transmission efficiency of this system are 5.811 W, 4.892 W, and 84.20%, respectively. In Fig. 25 (c), the waveform corresponds to Design-2, where the peak-to-peak voltage of the AC input is 97.44 V. The input power, output power, and transmission efficiency of this system are 5.809 W, 5.073 W, and 87.32%, respectively.

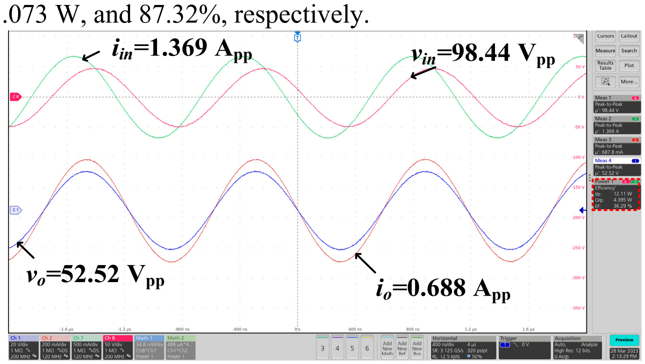

(a) 4-coil domino WPT system with conventional design

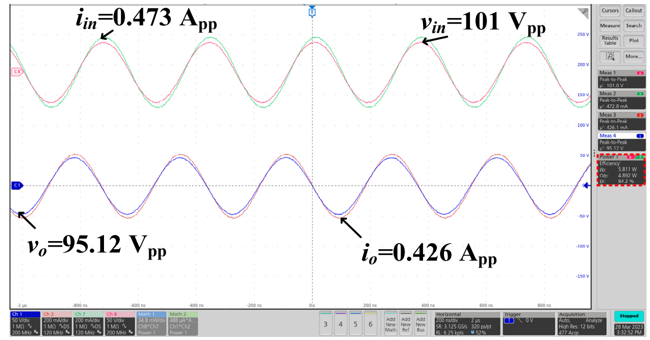

(b) 4-coil domino WPT system with Design-1

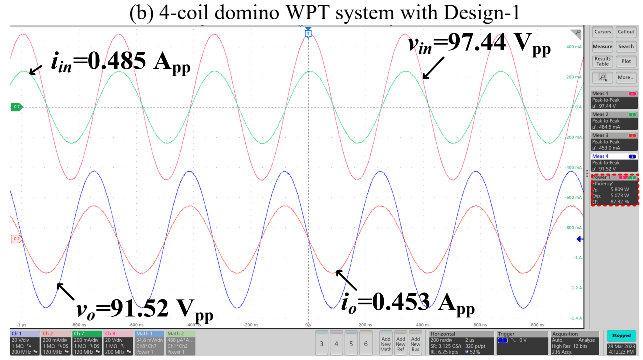

(c) 4-coil domino WPT system with Design-2

Fig. 25. Time-domain waveforms of the 4-coil domino WPT systems operating at the maximum efficiency point.

In Fig. 26 (a)-(d), the efficiency-normalized frequency plots of domino systems with various load conditions are evaluated. Fig. 26 (a) shows the efficiency curves of domino WPT systems with 50 Ω load. The WPT system with conventional design, Design-1, and Design-2 achieve highest efficiency of 35.37%, 67.69%, and 74.76%, respectively. Fig. 26 (b) shows the efficiency curves of domino WPT systems with 150 Ω load. The WPT system with conventional design, Design-1, and Design-2 achieve highest efficiency of 33.56%, 82.66%, and 86.16%, respectively. Fig. 26 (c) shows the efficiency curves of domino WPT systems with 250 Ω load. The WPT system with conventional design, Design-1, and Design-2 achieve highest efficiency of 27.54%, 83.64%, and 86.96%, respectively. Fig. 26 (d) shows the efficiency curves of domino WPT systems with optimal load. The WPT system with conventional design, Design-1, and Design-2 achieve highest efficiency of 36.66%, 83.65%, and 87.07%, respectively. These results reveal that Design-2 consistently outperformed the other designs, achieving the highest efficiency in all load conditions tested.

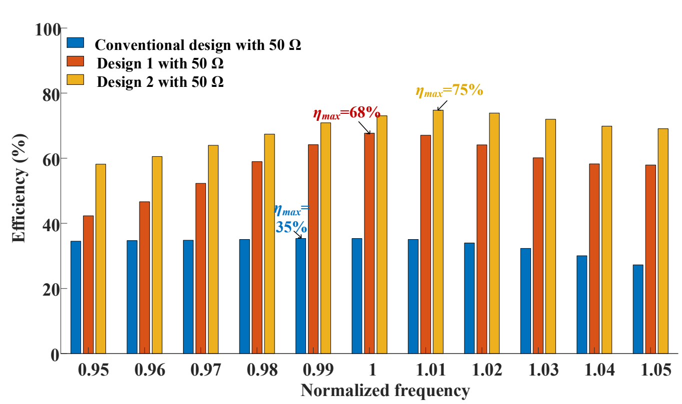

(a) With 50 Ω load resistance

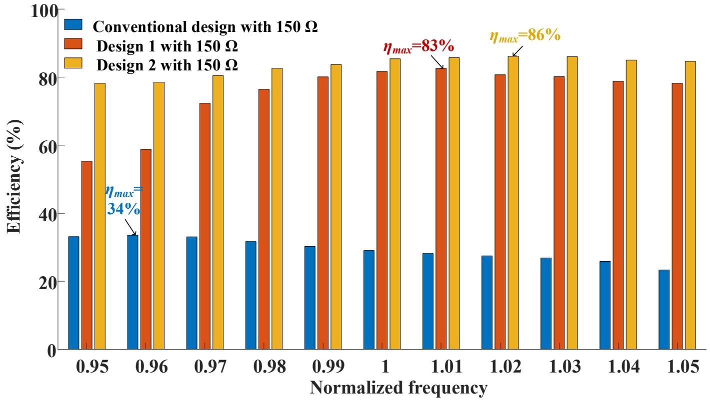

(b) With 150 Ω load resistance

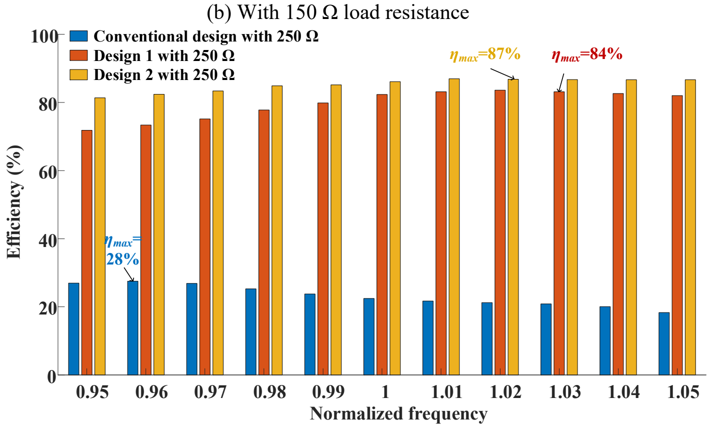

(a) With 250 Ω load resistance

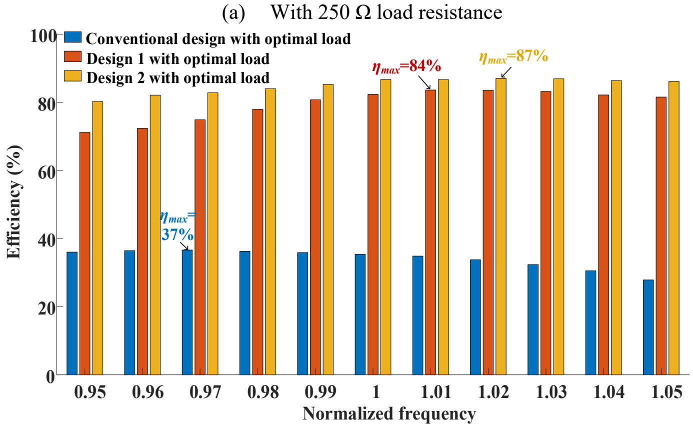

(d) With optimal load

Fig. 26. Transmission efficiencies of the 4-coil domino system with difference loads.

V. Conclusion

A new structure of PCB resonators based on two co-axially arranged PCBs separated by a small airgap to reduce inter-winding capacitance and the adoption of air-trenches between adjacent turns to reduce intra-winding capacitance is proposed and evaluated. An accurate distributed circuit model has been adopted to study the impedance and phase characteristics of a conventional resonator and two proposed resonators. The comparative study confirms that the new structure could lead to significant improvements in the quality factor, resonant frequency, and transmission efficiency. Compared with the conventional resonator, the new structure increases the Q factor from 37 to 199, and the resonant frequency from 879 kHz to 2.96 MHz. In the same domino wireless power transfer system, the transmission efficiency is increased from 37% to 87%.

VI. Acknowledgement

The authors would like to thank Dr. Yaoran Fang, Dr. Jialong Qu, and Dr. Jiali Zhou for their valuable discussions and assistance.

References

[1] Frank Toich, “A short history of the evolved power supply,” *Kepco Currents*, vol. 9, No.1 1988. [online] viewed on 29/9/2022, https://www.kepcopower.com/newsevo.htm.

[2] S.Y.R. Hui and S.C. Tang, “Coreless printed-circuit board transformers for signal and energy transfer, *IEE Electronics Letters* vol.34, no. 11, pp. 1052–1054, May 1998.

[3] S.Y. Hui and S.C. Tang; ‘Method of operating a coreless printed-circuit-board (PCB) transformer”, European Patent EP0935263B1, filed 3 Feb. 1999, granted 26 May 2004

[4] B. Ackermann Bernd; E. Waffenschmidt, “Size advantage of coreless transformers in the MHz range,” *European Power Electr. Conf.* (*EPE*) *2001*, paper PP00456.

[5] S.Y. Hui, H. Chung, and S.C. Tang, “Coreless Printed Circuit Board (PCB) Transformers for Power MOSFET/IGBT Gate Drive Circuits,” *IEEE Trans. on Power Electron*, Vol: 14 Issue: 3, Page(s): 422 –430, May 1999

[6] S.C. Tang S.Y. Hui; H. Chung, “Coreless planar printed-circuit-board (PCB) transformers – a fundamental concept for signal and energy transfer”, *IEEE Trans. on Power Electron*, Vol: 15 Issue: 5, Page(s): 931 –941, Sept 2000

[7] Infineon 1ED020I12-F2 Single IGBT Driver IC Data sheet, Rev.2.1, 2017-09-27.

[8] S. Zeltner, M. Billlmann and M. Marz, “An isolating IGBT half bridge driver with embedded magnetics, Fraunhofer Institute of Integrated Systems and Device Technology, , [online] 4 Oct. 2022, https://www.iisb.fraunhofer.de/content/dam/iisb2014/en/Documents/Research-Areas/vehicle_electronics/Publications/Isolating_Halfbridge_Driver_Module_Embedded_Magnetics_2004_IISB.pdf

[9] W. Frank, B. Strzalkowski and U. Jansen, “Coreless transformer provides innovative features: The expansion of the EiceDRIVER-family,” *Infineon Technologies, Germany [online] 4 Oct. 2022* , https://www.infineon.com/dgdl/Infineon-Coreless_Transformer_Bodo-ART-v1.0-en.pdf?fileId=db3a304412b407950112b40b54430787

[10] M. Glandalla, M. Grasso, S. Martino and M. Passoni, “”Planar transformer arrangement”, US patent US 7414507B2, Aug. 19, 2008.

[11] M. de Rooji, W. Huber and W. Burdick, Jr., “Planar, high voltage embedded transformer for analog and digital data transmission”, US 7915992B2, Mar. 29, 2011

[12] C. Jean-Paul and G. Bernard, “Capteur ferroviaire á transformateur sans noyau á haute isolation galvanique”, European Patent EP2348516A1, 27 July 2011

[13] S.Y.R. Hui, Semiconductor transformer”, US patent US 8049301 B2, Nov. 1, 2011.

[14] O. Spro et la, Optimized design of multi-MHz frequency isolated auxiliary power supply for gate drivers in medium-voltage converters”, *IEEE Trans. on Power Electron*, Vol: 35 Issue: 9, Page(s): 9494 –9509, Sept 2020

[15] O. Spro, F. Mauseth and D. Peftitsis, “High-voltage insulation design of coreless, planar PCB transformers for multi-MHz power supplies”, *IEEE Trans. on Power Electron*, Vol: 36 Issue: 8, Page(s): 8658 –8671, Aug 2021

[16] S.Y. R. Hui and C. Zhang, “Wireless power transfer system”, US patent US 10573455, Feb. 25, 2020

[17] C.K. Lee, S.Y.R. Hui and J. Qu, “Wireless power transfer system”, US patent US 10923957, Feb. 16, 2021

[18] J. Qu, L. He, N. Tang, and C. Lee, “Wireless power transfer using domino resonator for 110-kV power grid online monitoring equipment,” *IEEE Trans. Power Electron*., vol. 35, no. 11, pp. 11380–11390, Nov. 2020.

[19] Y. Fang, et la, “Quasi-static modeling and optimization of two-layer PCB resonators in wireless power transfer systems for 111-kV power grid

online monitoring equipment", *IEEE Trans. Ind. Electron*., vol.69. No.2, pp:1400-1410

[20] J. Qu, S. Kiratipongvoot, C. K. Lee, and N. Tang, "An integrated printed-circuit-board resonator design for inductive power transfer system," in *IEEE Energy Convers. Congr. Expo.*, ECCE, Portland, OR, USA, 2018, DOI 10.1109/ECCE.2018.8558378, pp. 2021–2025.

[21] K. Chen and Z. Zhao, "Analysis of the double-layer printed spiral coil for wireless power transfer," *IEEE J. Emerg. Sel. Top. Power Electron*., vol. 1, no. 2, pp. 114-121, June 2013.

[22] Z. Yi et al, "Self-resonant antisymmetric planar coil for compact inductive power transfer system avoiding compensation circuits," *IEEE Trans. Power Electron*., vol. 36, no. 5, pp. 5121-5134, May 2021.

[23] R. Qin et al., "A 6.6-kW high-frequency wireless power transfer system for electric vehicle charging using multilayer nonuniform self-resonant coil at MHz," *IEEE Trans. Power Electron.*, vol. 37, no. 4, pp. 4842-4856, Apr. 2022.

[24] K. Li and S.Y.R. Hui, "Printed-circuit-board inductive-capacitive resonators for high frequency operation", *Singapore provisional patent application number* 10202300104Y, 13 January 2023.

[25] K. Li, J. Wu, M. Wang, A. Yucel, and S.Y.R. Hui, "A sandwiched structure for cost-effective printed-circuit-board wireless power resonators", *IEEE Appl. Power Electr. Conf*., March 2023, Orlando, USA.

[26] X. Huang, KDT Ngo, G Bloom, "Design techniques for planar windings with low resistances", Proceedings of 1995 *IEEE Applied Power Electronics Conference and Exposition*, 5-9 March 1995, Dallas, TX, USA, 1995, Vol.2, p.14-539

[27] S. R. Cove et. al., "Improving wireless power transfer efficiency using hollow windings with track-width-ratio," *IEEE Trans. Power Electron*., vol. 31, no. 9, pp. 6524-6533, Sept. 2016.

[28] Y. Fang. "Multiple harmonic analysis and electromagneto-quasistatic modeling for high frequency resonant converters with simulation-driven design optimization". (Thesis). University of Hong Kong, Pokfulam, Hong Kong SAR., 2021